Phosphorene Nanoribbon-Augmented Optoelectronics for Enhanced Hole Extraction

Thomas J. Macdonald*[1,2], Adam J. Clancy[2,3], Weidong Xu[1], Zhongyao Jiang[4], Chieh-Ting Lin[1], Lokeshwari Mohan[4,5], Tian Du[4], Daniel D. Tune[6], Luis Lanzetta[1], Ganghong Min[1], Thomas Webb[7], Arjun Ashoka[8], Raj Pandya[8], Vasiliki Tileli[9], Martyn A. McLachlan[4], James R. Durrant[1,10], Saif A. Haque[1], and Christopher A. Howard[3]

1. Dr. T.J. Macdonald, W. Xu, Dr. C-T. Lin, Dr. L. Lanzetta, Ganghong Min, Prof. J.R. Durrant, Prof. S.A. Haque

Department of Chemistry and Centre for Processable Electronics, Imperial College London, London, W12 0BZ, United Kingdom

Corresponding Author E-Mail: t.macdonald@imperial.ac.uk

2. Dr. T.J. Macdonald, Dr. A.J. Clancy

Department of Chemistry, University College London, 20 Gordon St, London, WC1H 0AJ, United Kingdom

3. Dr. A.J. Clancy, Prof. C.A. Howard

Department of Physics & Astronomy, University College London, Gower St, London, WC1E 6BT, United Kingdom

4. Z. Jiang, L. Mohan, Dr. T. Du, Prof. M.A. McLachlan

Department of Materials and Centre for Plastic Electronics, Imperial College London, London, W12 0BZ, United Kingdom

5. L. Mohan

School of Engineering and Materials Science, Queen Mary University of London, London E1 4NS, United Kingdom

6. Dr. D.D Tune

International Solar Energy Research Center Konstanz e.V., Rudolf-Diesel-Straße 15, D-78467, Konstanz, Germany

7. T. Webb

Advanced Technology Institute, Department of Electrical and Electronic Engineering, University of Surrey, Guildford, Surrey, GU2 7XH, UK

8. A. Ashoka, Dr. R. Pandya

Cavendish Laboratory, University of Cambridge, J.J. Thomson Avenue, CB3 0HE, Cambridge, UK

9. Dr. V. Tileli

Institute of Materials, École Polytechnique Fédérale de Lausanne, 1015 Lausanne, Switzerland

10. Prof. J.R. Durrant

SPECIFIC IKC, College of Engineering, Swansea University, Swansea, SA2 7AX, United Kingdom

Keywords: phosphorene, phosphorene nanoribbons, perovskite, perovskite solar cells, nanomaterials

TOC

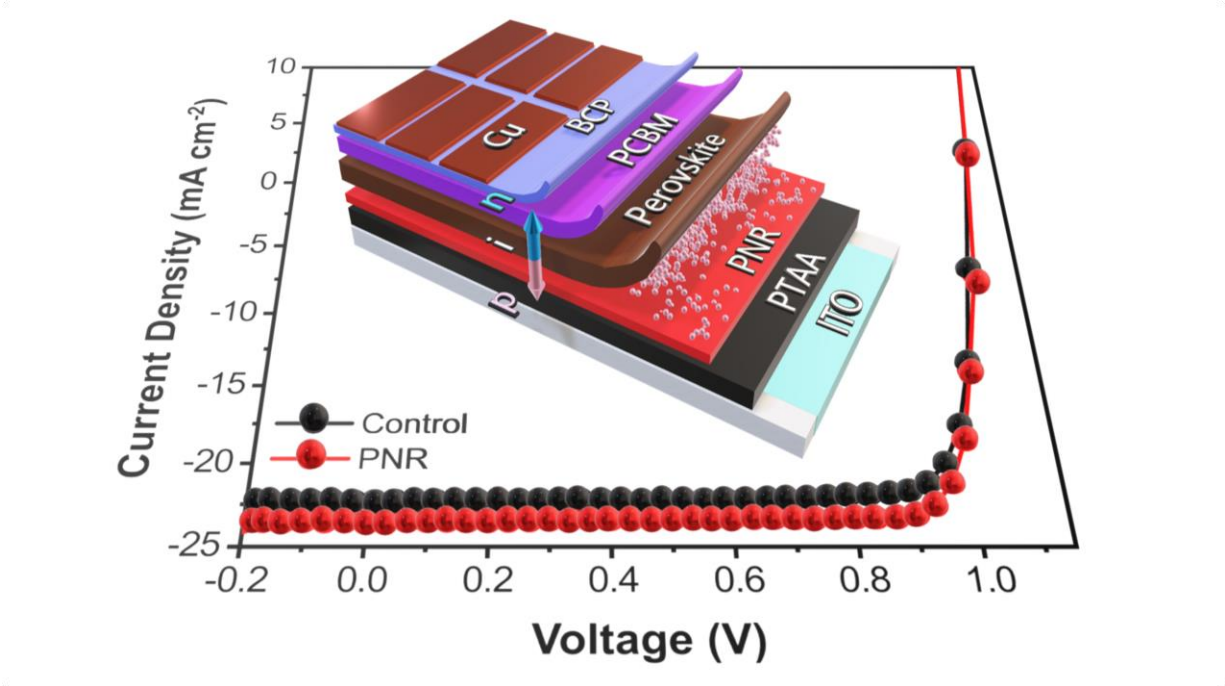

Abstract

Phosphorene nanoribbons (PNRs) have been widely predicted to exhibit a range of superlative functional properties, however since they have only recently been isolated, these properties are yet to be shown to translate to improved performance in any application. PNRs show particular promise for optoelectronics, given their predicted high exciton binding energies, tunable band gaps, and ultrahigh hole mobilities. Here, we verify the theorized enhanced hole mobility in both solar cells and space-charge-limited-current devices, demonstrating the potential for PNRs improving hole extraction in universal optoelectronic applications. Specifically, PNRs are demonstrated to act as an effective charge-selective interlayer by enhancing hole extraction from polycrystalline methylammonium lead iodide ($MAPbI_3$) perovskite to the poly(triarylamine) semiconductor. Introducing PNRs at the hole-transport/ $MAPbI_3$ interface achieves fill factors above 0.83 and efficiencies exceeding 21% for planar p-i-n (inverted) perovskite solar cells (PSCs). Such efficiencies are typically only reported in single-crystalline $MAPbI_3$-based inverted PSCs. Methylammonium-free PSCs also benefit from a PNR interlayer, verifying applicability to architectures incorporating mixed

perovskite absorber layers. Device photoluminescence and transient absorption spectroscopy are used to demonstrate that the presence of the PNRs drives more effective carrier extraction. Isolation of the PNRs in space-charge-limited-current hole-only devices improves both hole mobility and conductivity; demonstrating applicability beyond PSCs. This work provides primary experimental evidence that the predicted superlative functional properties of PNRs indeed translate to improved optoelectronic performance.

Introduction

Phosphorene is a monolayer of black phosphorus where its tunable, direct bandgap, high-carrier mobility, and anisotropic characteristics make it a promising candidate for a range of applications.[1–8] While 2D materials in sheet form, such as phosphorene, are widely investigated, their 2D-ribbon counterparts offer new opportunities given their width-induced confinement effects and edge states that could enable further tuning of properties and emergent exotic phenomena.[9–14] As a result, graphene nanoribbons are now a widely studied class of materials. Despite the motivation of many theory papers predicting exciting properties, synthetic routes for phosphorene nanoribbons (PNRs) are only recently appearing in the literature.[8,14–17] Early attempts focused on lithography[15–17] of 2D phosphorene, creating singular ribbons with limited control over geometry and thus properties. In 2019 an intrinsically scalable, top-down synthesis of stable PNR liquid dispersions was demonstrated.[14] The produced ribbons are discrete, atomically-flat single crystals, cut perfectly along the zigzag crystallographic orientation with uniform widths ranging between ~4–50 nm and lengths of up to 75 µm, opening up applications beyond individual nanoelectronic devices.[8,14] During the preparation of this manuscript, Yu *et al*.[18] used PNRs as a protective layer in lithium-ion batteries to prevent lithium dendrite growth. Interestingly, it was the chemical edge states of the ribbons that were proposed to react with lithium to provide a protective layer, rather than the intrinsic properties of the PNRs themselves.

Therefore, despite the predicted superlative properties of PNRs discussed in theoretical studies, there is still no experimental evidence that their electronic properties indeed translate to improved functionality in application. For example, an electronic property of interest is their predicted high hole mobilities,[9] giving PNR films potential as novel hole transport materials (HTMs) in photovoltaic (PV) devices.

Perovskite solar cells (PSCs) have rapidly emerged as one of the most promising candidates for future PV due to their visible to near-infrared absorption,[19,20] long diffusion lengths,[21,22] electronic and physical tunability,[23,24] high efficiency,[25,26] and low manufacturing costs.[27,28] One major advantage of PSCs is their solution processability, which has generated further avenues of improvement by the incorporation of nanomaterials.[29–31] The most successful HTMs in PSCs are either small organic molecules or semiconducting polymers, and this has represented one of the major challenging components for further enhancements in both device stability and efficiency. Capitalizing on PNRs in PSCs will depend heavily on their ability to transport holes and thus requires sufficient pairing with other constituents in the device architecture to prevent the formation of a potential barrier, such as at the HTM/perovskite interface. Analogous to phosphorene, the conduction and valence band of PNRs is thickness dependent, thus enabling energy level matching with the other components within a PSC.[32] Studies exploiting phosphorene or black phosphorus in PSCs at the hole transport layer (HTL)/perovskite[33,34] or electron transport layer (ETL)/perovskite interface[35,36] is to date limited, where a majority of the work has involved black phosphorus quantum dots. In 2020, Zhang *et al*.[37] demonstrated synergistic cascade carrier extraction *via* dual interfacial positioning of black phosphorene in *n-i-p* structured PSCs and achieved an efficiency of 19.8%. The anisotropic nature of black phosphorene was utilized to tune proper thicknesses at both the ETL/perovskite and HTL/perovskite interfaces, resulting in synergistic enhancements

of charge transfer and charge collection. Despite this impressive result, no examples of layered phosphorene have been studied in *p-i-n* structured (inverted) PSCs.

Here, we introduce the use of PNRs in optoelectronics in which we investigate their applicability as a HTM with a poly(triaryl amine) (PTAA) semiconductor in inverted PSCs. The addition of PNRs at the HTL/perovskite interface achieves fill factors above 0.83 and efficiencies exceeding 21%. We couple device photoluminescence (PL) and femtosecond transient absorption spectroscopy (fs-TAS) to demonstrate that spin coating a PNR interlayer at the HTL/perovskite interface provides fast and efficient hole extraction from the absorber layer to PTAA. We also fabricate space-charge-limited-current (SCLC) hole-only devices and demonstrate improvements in both mobility and conductivity when PNRs are present. This work reveals a promising use of PNRs in perovskite optoelectronics and also demonstrates their potential for universal applicability in next-generation optoelectronic devices. Using a range of experimental processing and characterization, we demonstrate that the predicted superlative properties of PNRs indeed translates to improved functionality in application.

Results and Discussion

PNRs were produced as per our previous report and dispersed in N-Methyl-2-pyrrolidone (NMP) or dimethylformamide (DMF).[14] Brief sonication of the LiP_8 salt in anhydrous NMP and mild centrifugation yields a yellow, cloudy solution of PNRs, with strong absorption at ~380 nm and a broad scattering background from dispersed nanoscale species (**Figure 1**a). The band gap (E_g) of the PNRs is ~1.97 eV, calculated from cyclic voltammetry (Figure S1), which correlates well to previously reported phosphorene.[38] The synthesized PNRs formed have a distribution of widths and lengths (typically 50 nm to 10 μm in length and 5 to 50 nm in width) consistent with our previous report[14]. A TEM micrograph of an individual ribbon is shown in Figure 1b and a false colored version of this data, with the PNR highlighted in red in

Figure S2. Our measurements also revealed that the highest occupied molecular orbital (HOMO) for the PNRs is ~5.41 eV, which prompted us to investigate this material's hole extraction ability in PSCs. Since the PNRs are dispersed in polar aprotic solvents, this study focused on inverted PSCs where PNRs were placed at the HTL/perovskite interface. Placing PNRs between the perovskite/HTL in an *n-i-p* architecture would compromise the perovskite layer due to its own solubility in polar aprotic solvents. The effect of PNR hole extraction was examined using our established inverted architecture with PTAA as the HTL and methylammonium lead iodide ($MAPbI_3$) as the perovskite absorber material.[39] The band diagram for the proposed hole extraction mechanism from $MAPbI_3$ to the respective HTLs is shown in Figure 1d. All processing was carried out in a nitrogen filled glovebox where films were subject to additional spin coating steps and gentle heating/vacuum to remove excess NMP or DMF (see experimental section). Prior to device fabrication, the presence of PNRs on the PTAA films was confirmed by Raman spectroscopy as shown in Figure 1c, although direct visualization of PNRs on PTAA was not feasible through probe microscopy due to the intrinsic roughness of the substrate (Figure S3). In addition, Raman spectroscopy for LiP_8 crystals from Li/NH_3 treatment of black phosphorus and neat PTAA films are shown in Figure S4. To investigate whether the PNRs would affect the morphology or crystallization of the perovskite layer, X-ray diffraction (XRD) and scanning electron microscopy (SEM) were used to check the $MAPbI_3$ after deposition on PTAA. XRD of $MAPbI_3$ films with and without PNRs on PTAA is shown in Figure S5a, where the 110 diffraction peak at 14.2 °2θ shows no change in peak full-width-half-maximum (FWHM) or peak shifting, supporting that PNRs do not influence the crystallization of the perovskite layer. Furthermore, Figure S5b shows an SEM image of the $MAPbI_3$ on PNR/PTAA substrate. The topography of $MAPbI_3$ is identical to our previous report when deposited on PTAA,[35] suggesting that the PNR layer does not induce any issues with the morphology of the $MAPbI_3$ film.

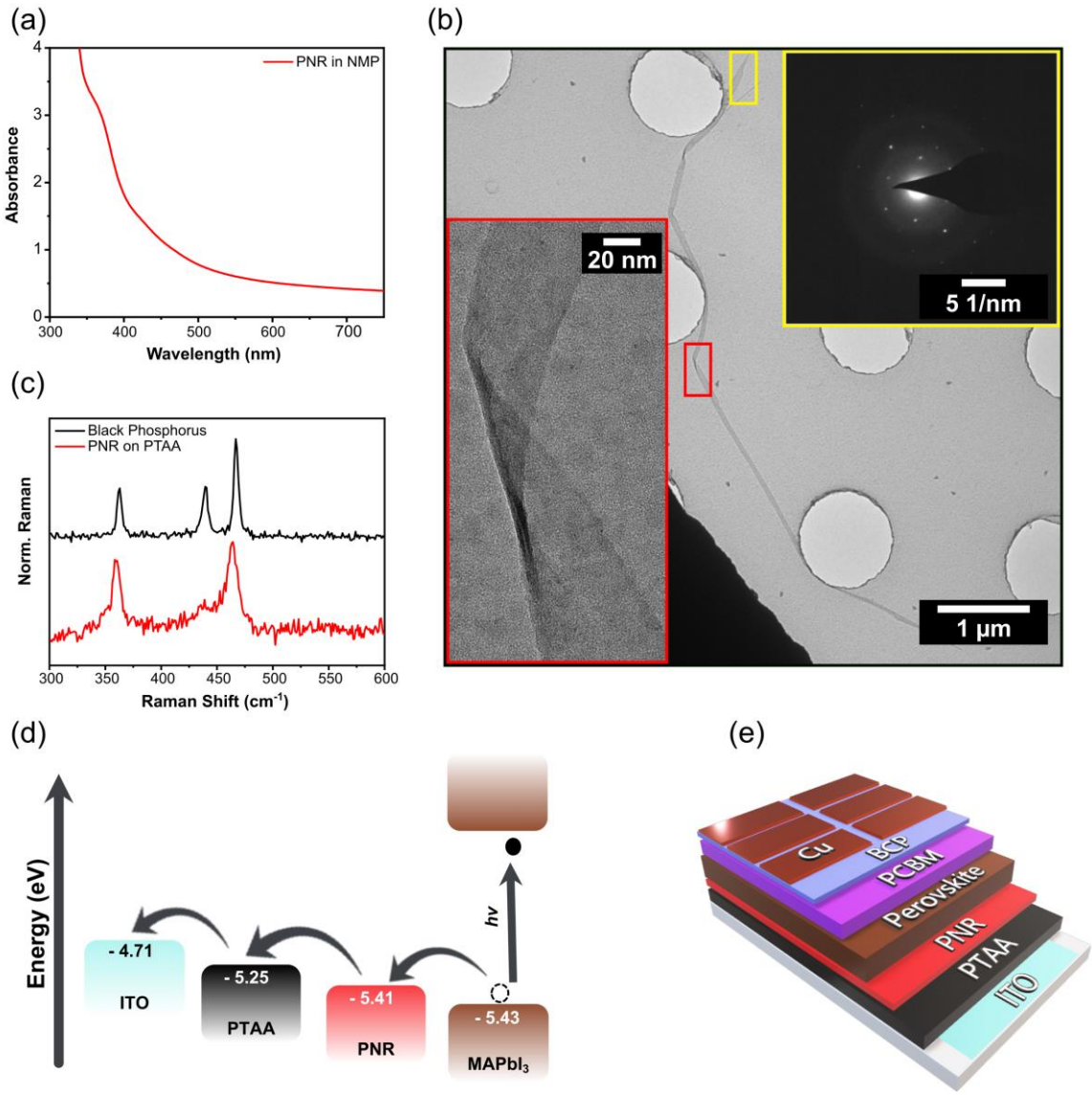

Figure 1. (a) UV-visible spectra of PNR solution showing a strong peak at ~380nm and the exponential background typical of scatter from objects of comparable length scale to the incident light. (b) TEM micrograph of an individual PNR deposited on holey carbon grid. Inset (red) shows zoom of isolated PNR and inset (yellow) shows SAED pattern. False colored version with the PNR highlighted in red is provided in Figure S2. (c) Normalized Raman spectra (785 nm excitation) of black phosphorus and PNR on PTAA. (d) Energy diagram schematic of hole transfer from $MAPbI_3$ to PNR, PTAA and ITO. (e) Inverted PSC device stack with PNRs deposited between PTAA and perovskite.

$MAPbI_3$ was sandwiched between PNR/PTAA as the HTL and fullerene derivative [6,6]-phenyl-C_{61}-butyric acid methyl ester (PCBM) as the ETL. An ultrathin layer of poly(9,9-bis(3'-(N,N-dimethyl)-N-ethylammoinium-propyl-2,7-fluorene)-alt-2,7-(9,9-dioctylfluorene))dibromide (PFN) was added on top of the PTAA to improve wetting[40] and bathocuproine (BCP) was added between the PCBM and copper electrode to minimize non-

radiative recombination at the ETL/Cu interface (Figure 1e).[41] Given that the direct band gap of PNRs is thickness dependent, it is vital to control the number of spin coated cycles of PNRs on PTAA in order to match the energy levels and optimize device performance. PNRs were optimized with respect to PV performance (Figure S6 and Table S1) and are labelled as PNR-1,2,3, or 4 which represents the number of spin coated cycles between the HTL/perovskite interface. A summary of the PV parameters of the PSCs incorporating PNR-1 is presented in Table 1, which show that the average power conversion efficiency (PCE) values improved from 18.66 ± 0.43% (control) to 20.12 ± 0.51% (PNR), due to improvements in all PV parameters; short-current density (J_{SC}), open-circuit voltage (V_{OC}), and fill factor (FF). When PNR-2,3, and 4 were employed, the average PCE decreased to 16.81 ± 0.39%, 16.05 ± 0.42%, and 12.68 ± 0.20%, respectively. Despite the lower PCE, the average J_{SC} still remained higher than the control cells except when PNR-4 was employed, where the PSCs showed a decrease in J_{SC} to 18.29 ± 0.16 mA cm^{-2}. We attribute this 21% decrease in J_{SC} to the increased thickness of the PNR layer, which possibly impeded charge extraction from the PNRs to the PTAA. This was further supported in Figure S7 that shows a current-voltage (*J*–*V*) curve for PSCs incorporating a 5th cycle of PNRs (PNR-5), further decreasing the J_{SC} with respect to the control and PNR-4 PSCs. The V_{OC} was also reduced by ~100 mV with respect to control devices when PNR-2 or more were employed. The significant decrease in voltage can be attributed to an energy level mismatch with respect to the anisotropic nature of the PNRs,[37] where PNR-1 provided the most suitable conditions for optimized PSCs. Although the FF remained over 0.7 for all PNR devices, there was a notable decrease as the number of PNR cycles increased above 3, which can be attributed to parasitic resistive losses leading to reduced charge carrier extraction. Lower PNR contents (from diluted solutions) were also investigated and shown to be less effective than PNR-1 conditions (see Table S2). This confirms that adding lower PNR contents does not further improve the PSCs, however additional layers of PNRs indeed lowers the performance.

Figure 2a shows a cross-sectional SEM image of the optimized PNR-1 PSC structure based on ITO/PTAA/PFN/PNR/$MAPbI_3$/PCBM/BCP/Cu, where the thickness of the $MAPbI_3$ is approximately 580 nm, consistent with previous work.[39,42] From here on, PNR will refer to the optimized PNR-1 PSCs. *J*–*V* curves of champion devices with and without PNRs are shown in Figure 2b. Champion control devices measured with a reverse scan show a PCE of 19.60%, J_{SC} of 22.30 mA cm^{-2}, V_{OC} of 1.089 V, and FF of 0.807. Devices incorporating the PNRs exhibited a PCE of 21.14%, J_{SC} of 23.33 mA cm^{-2}, V_{OC} of 1.093 V, and FF of 0.829. In order to only focus on the effect of the PNR interlayer, no additional passivation strategies were employed. We note that the use of PNR interlayers enabled PCEs in polycrystalline $MAPbI_3$-based inverted PSCs, comparable to those typically only reported in single-crystal devices.[43] Given that hysteresis changes dynamically depending on the measurement parameters,[44] plots of the maximum power point (MPP) tracking of the devices are shown in the inset of Figure 2b and show stabilized power outputs (SPOs) of 18.90% (control) and 20.10% (PNR). Forward and reverse *J*–*V* scans are shown in Figure S8 of devices with and without PNRs, where they remain essentially unchanged – a recognized advantage of using the inverted architecture.[45,46] Integrated current densities derived from the external quantum efficiency (EQE) are shown in Figure 2c and match the J_{SC} from the *J*–*V* curves, excluding any spectral mismatch as highlighted in previous work.[47] Furthermore, 1000 hour stability measurements of the devices held at open-circuit conditions is shown in Figure S9, demonstrating that the introduction of the PNRs does not impede the device stability. A statistical distribution of all PV parameters for ~70 devices (control and PNR) is shown in Figure 2d. Although all average PV parameters were improved for PSCs with the PNR interlayer, the most notable improvements were in the J_{SC}, along with a slight improvement in V_{OC} and FF. The improvement in FF for the PSCs can be partly attributed to the reduced average series resistance (R_s) for the PNR devices (2.97 ± 0.45 Ω cm^2) compared with those

of the control devices ($3.89 \pm 0.37\ \Omega\ cm^2$). To investigate the improved PV parameters further, J_{SC} and V_{OC} were measured as a function of light intensity for PSCs with and without PNRs. The incident light intensity (I) was varied from 100 mW cm^{-2} (1 sun) to 1 mW cm^{-2} (0.01 sun) and the power law dependence of J_{SC} with I is shown in Figure S10, in which the logarithm of J_{SC} and I are plotted. PSCs with and without PNRs show α values close to 1, where an α of 0.97 (control) and 0.98 (PNR), suggest minimal space charge limited behavior.[48] It is possible that the addition of the PNRs provides a more favorable interface between the HTL/$MAPbI_3$, which plays a role in minimizing recombination in the PSCs, and this is also supported by the high FFs and reduced R_s.[49] To further investigate the recombination processes, the dependence of V_{OC} on I is shown in Figure 2e. For bimolecular recombination, the slope of V_{OC} *vs*. ln(I) is equal to, k_BT/e, where k_B is Boltzmann constant, T is temperature, and e is the elementary charge. However, for monomolecular recombination (trap-assisted recombination), the electron and hole densities at open circuit would each be proportional to I, and the slope of V_{OC} *vs*. ln(I) is given by $2k_BT/e$.[50] While this provides a straightforward method of distinguishing bimolecular and monomolecular recombination, the ideality factor (n_{ID}) is a useful tool that can be used to assess intermediate recombination processes where the V_{OC} dependence on ln(I) gives the slope $n_{ID}k_BT/e$.[51,52] In the absence of monomolecular recombination, the ideal diode equation applies where n_{ID} equals 1. On the other hand, in the presence of monomolecular recombination, n_{ID} can increase up to a value of 2.[53–55] Figure 2e shows an n_{ID} of 1.64 (control) and 1.54 (PNR), demonstrating that the PNRs reduced monomolecular recombination, leading to more ideal diode characteristics. This reduction in trap-mediated processes also supports the slightly higher V_{OC} measured for the PSCs with PNRs (Figure 2d).

Given the growing concerns regarding the stability of PSCs incorporating methylammonium (MA),[56,57] MA-free devices with and without PNRs were prepared using formamidinium and cesium cations, $FA_{0.95}Cs_{0.05}PbI_3$. In line with our findings discussed above, PSCs incorporating PNR-1 show improved PV performance with respect to control cells. PSCs based on $FA_{0.95}Cs_{0.05}PbI_3$ achieved average PCEs of 18.93 ± 0.47% (control) and 20.13 ± 0.43% (PNR) and a statistical distribution of the PV parameters is shown in Figure S11. Such efficiencies are in line with previous reports incorporating an MA-free absorber layer in inverted PSCs.[58,59] The improvement seen for $FA_{0.95}Cs_{0.05}PbI_3$ confirms that the introduction of PNRs in PSCs is not limited to $MAPbI_3$ (or its bandgap) and can be complementary to other systems and/or possible architectures.

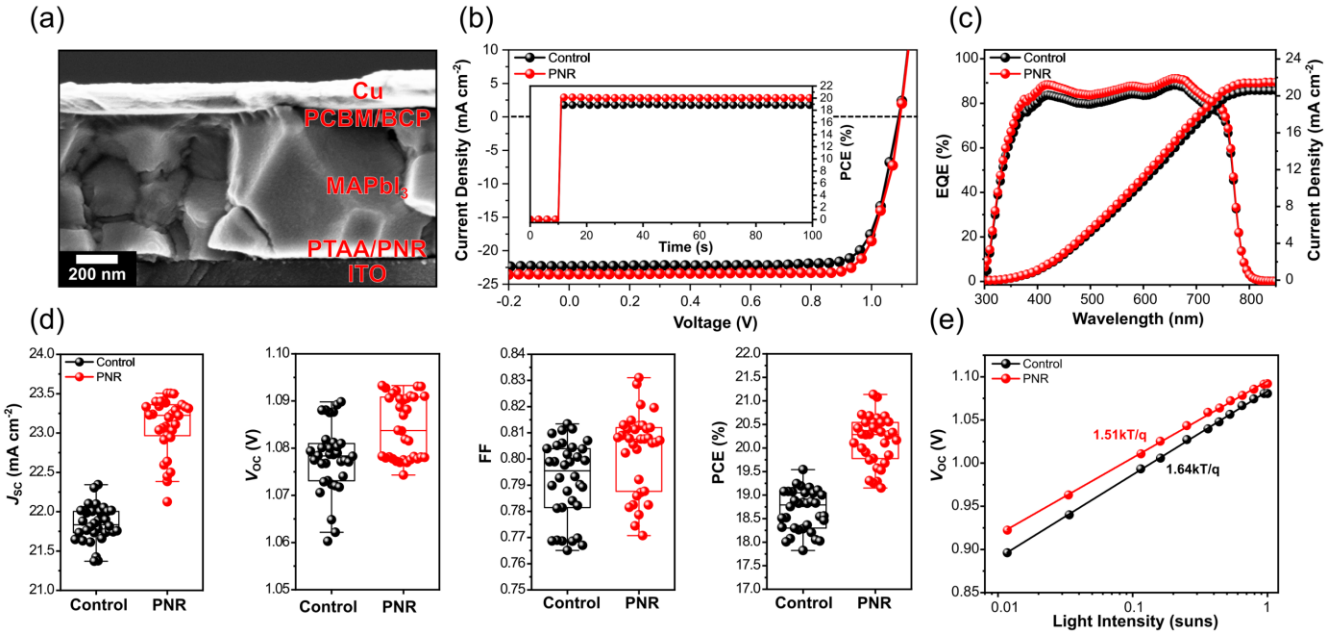

Figure 2. (a) Cross-sectional SEM of PSC with PNRs, (b) *J–V* curve of champion PSCs with and without PNRs (inset showing stabilized PCEs), (c) EQE and integrated current density of control and PNR PSCs, (d) PV parameters as statistical distribution for ~70 PSCs with and without PNRs, (e) semi-log plot of V_{OC} as a function of light intensity.

Table 1. Photovoltaic parameters extracted from the J-V curves for control and PNR inverted PSCs. Champion devices are highlighted in bold.

Device	J_{SC} (mA cm^{-2})	V_{OC} (V)	***FF***	**PCE** (%)	**SPO (%)**
Control	**22.30** 21.85 (+/- 0.23)	**1.089** 1.078 (+/- 0.007)	**0.807** 0.792 (+/- 0.015)	**19.60** 18.66 (+/- 0.43)	**18.90**
PNR	**23.33** 23.11 (+/- 0.35)	**1.093** 1.084 (+/- 0.007)	**0.829** 0.803 (+/- 0.015)	**21.14** 20.12 (+/- 0.51)	**20.10**

To understand more about the effect that the PNRs had on the hole transport properties, we isolated the PNRs from the absorber material and prepared space-charge-limited-current (SCLC) hole-only devices with the configuration ITO/PEDOT:PSS/PTAA/Au and ITO/PEDOT:PSS/PTAA/PNR/Au. The *J*–*V* characteristics can be described by the SCLC with, $J(V) = (9/8)\epsilon\epsilon_0\mu V^2 / d^3$ where ϵ is the dielectric constant (3 for organic films) and *d* is the film thickness.[60–63] The mobilities of hole-only devices were extracted from Figure 3a as 1.08 × 10^{-4} cm^2 V^{-1} s^{-1} (control) and 2.76 × 10^{-4} cm^2 V^{-1} s^{-1} (PNR), consistent with previous values reported in the literature.[64,65] The improved mobility in the PNR devices suggests that hole extraction is improved and recombination minimized, consistent with the improved FF measured for PSCs with PNRs (Figure 2d). Furthermore, the direct current (DC) conductivity (σ_0) was extracted from the slope of the current–voltage (*I*–*V*) curve, $I = \sigma_0 A d^{-1} V$,[66] where A is the area of the sample and *d* is the thickness of the PTAA. The corresponding conductivities were extracted from Figure 3b as 9.25 × 10^{-7} S cm^{-1} (control) and 1.02 × 10^{-6} S cm^{-1} (PNR), which suggests that the PNRs reduced the series resistance in the PTAA, which is consistent with *J*–*V* characteristics of full devices. Therefore, it is expected that from the improved mobility and conductivity of devices incorporating the PNRs, charge carriers are more efficiently transported to the PTAA. The SCLC results demonstrate that the PNRs facilitate hole extraction without a perovskite absorber, further complementing their application in optoelectronics beyond PSCs.

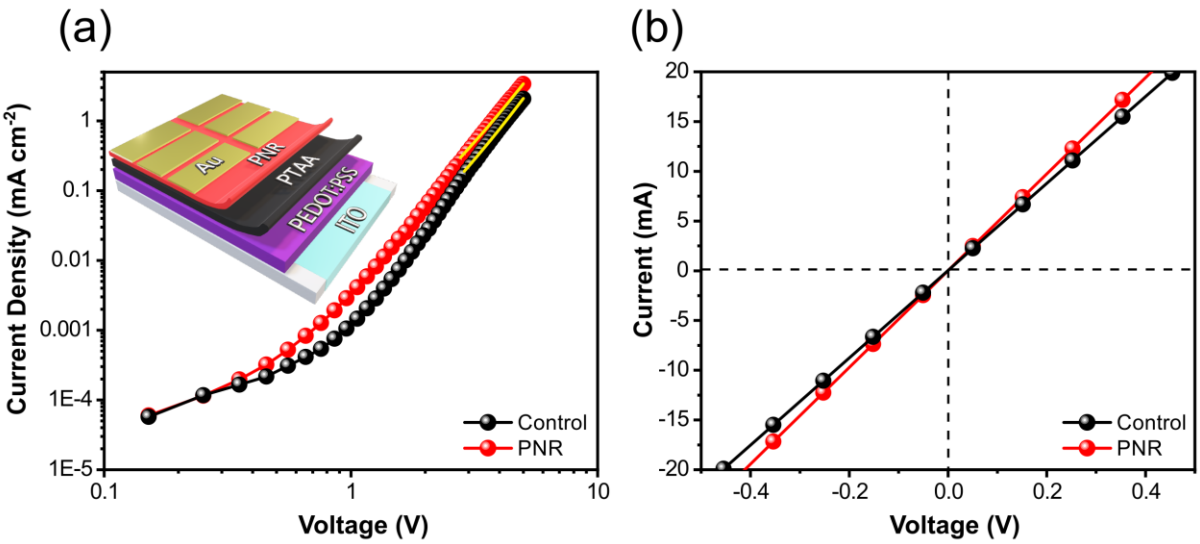

Figure 3. (a) Log-log *J-V* plot of hole-only SCLC devices with the architectures ITO/PEDOT/PTAA/Au and ITO/PEDOT/PTAA/PNR/Au. The yellow line represents the gradient of the fitted regions for mobility extraction. (b) *J-V* plot for conductivity extraction at the ohmic region for hole-only devices with the architectures ITO/PTAA/Au and ITO/PTAA/PNR/Au.

To investigate the effect that the PNRs had on the recombination and charge carrier extraction characteristics, we performed 1-sun equivalent photoluminescence (PL) spectroscopy for complete devices at both open-circuit (OC) and short circuit (SC) conditions. The device OC to SC quenching efficiency (PLQ_{OC-SC}) has been previously demonstrated as an effective figure-of-merit to assess the charge carrier extraction efficiency in PSCs, which is calculated as $PLQ_{OC-SC}=(PL_{OC}-PL_{SC})/PL_{OC}$.[67,68] **Figure 4**a shows that under OC condition, there is almost no difference in PL intensity of both control and PNR devices, demonstrating the same radiative recombination and quasi-fermi-level-splitting (QFLS).[69] This suggests that the PNRs do not introduce any additional interfacial recombination paths at the HTL/$MAPbI_3$ interface or change the properties of bulk $MAPbI_3$. Interestingly, under SC conditions devices with the PNRs show lower PL intensity, enhancing the PLQ_{OC-SC} from 0.91 (control) to 0.94 (PNRs). We also demonstrate that regardless of the excitation fluences (Figure S12), under SC conditions devices with PNRs show lower PL intensity. This implies PNRs have improved the charge extraction compared to the control PSCs which is in agreement with the improved PV parameters, J_{SC} and FF. W

In order to compare the charge extraction/separation behavior, steady-state PL and femtosecond transient absorption spectroscopy (fs-TAS) were used to probe the excited states in ITO/PTAA/PNR/$MAPbI_3$ films. Due to the air-sensitive nature of the PNRs, all films were sealed in a nitrogen filled glovebox before spectroscopic measurements were carried out. Prior to performing PL measurements, UV-visible spectroscopy of the films with and without PNRs was carried out and no notable changes in absorption were observed (Figure S13). In addition, the thickness of the layers in the control devices also remained unchanged – eliminating any inconsistences based on thickness (Figure S14). Steady-state PL of neat $MAPbI_3$, ITO/PTAA/$MAPbI_3$, and ITO/PTAA/PNR/$MAPbI_3$ is shown in Figure S15. The PL quenching efficiency was calculated as per our previous report,[30] where PNRs improved the quenching of the PTAA by 37%. We attributed this to improved charge extraction from the $MAPbI_3$ to the PNR/PTAA rather than increased surface recombination, since PNR devices also show improved V_{OC}. We further probed the effects of the PNRs by replacing PTAA with PMMA to investigate the quenching effects using an inert polymer with otherwise poor quenching efficiency. Figure S16 shows that the PNRs improve the quenching of the PMMA by 44%, demonstrating that the effectiveness of the PNRs is not limited to semiconducting polymers like PTAA. We now turn to fs-TAS, which is an optical technique used to determine the charge extraction properties.[21] Figure 4c represents the fs-TAS spectra at different delay times, demonstrating the spectral changes of the photobleaching (PB) between the films with and without PNRs. Neat $MAPbI_3$ fs-TAS spectra also at different delay times is shown in Figure S17 of the SI. The most prominent feature for all films is the negative optical density change (ΔOD) peaked at 758 nm, which can be attributed to PB at the band edge.[21] It is also noticeable that in the early time scale (< 450 fs) that there is a rising of negative PB signal at higher energy (751 nm), along with a decrease of the positive photoinduced absorption peak at 777 nm. These kinetic features can be assigned to hot carrier cooling at the band edge.[70] Right after the carriers are cooled, the PB peak reaches its maximum at the same

time for all films, and then starts to decay due to recombination of cooled carriers. To further understand the evolution of ΔOD as a function of time, we probed the decay kinetics of the band edge PB in a 6 ns range for neat $MAPbI_3$, ITO/PTAA/$MAPbI_3$, and ITO/PTAA/PNR/$MAPbI_3$ films. Figure 4d shows these PB decay kinetics; it is apparent that the presence of interlayers results in faster decay kinetics, assigned to hole extraction from $MAPbI_3$ to the interlayer. Decay kinetics with lifetimes of 15.5 ns (control) and 9.9 ns (PNR) are shown, indicating faster hole extraction from the $MAPbI_3$ to the PNRs when the pump fluence is 4 μJ cm^{-2}. All fs-TAS measurements were also repeated using a lower pump fluence of 0.8 μJ cm^{-2}, where the trend is clear and consistent with the previous conditions and faster hole extraction is observed in the PNR film (Figure S18). Figure 4b shows the proposed hole transfer schematic which are based on the charge extraction results obtained from Figure 4a and quantified from Figure 4d. To further verify the kinetics implied by the fs-TAS measurements, the PL decay kinetics were analyzed using an excitation of 635 nm and probe of 770 nm. The PL decays shown in Figure S19 were fitted with the biexponential function, $y = y_0 + A_1 e^{-\frac{x}{t1}} + A_2 e^{-\frac{x}{t2}}$.[71] We attribute τ_1 primarily to the hole extraction time at the HTL/ $MAPbI_3$ interface of 1.9 ns (control) and 1.5 ns (PNR). We attribute τ_2 primarily to the diffusion limited hole extraction time as bulk charges takes time to reach HTL/MAPI interface before been transferred (we note the extraction lifetimes determined from fs-TAS should be an average of these two TCSPC decay phases). In addition to the faster extraction times, A_1 is also larger for the PNR than the control films which is indicative of more efficient hole extraction of the former (Table S3). These results are in good agreements with the steady-state PL and fs-TAS data. Although defect passivation of the perovskite layer remains a popular argument for improved PSC performance, any potential passivation effects from the PNRs at the interface do not appear to play a significant role here. Improved hole extraction is indicated by the steady-state and device PL and the time-resolved decays from TCSPC and TAS, collectively. While high hole field-effect mobility has led to predictions of

efficient hole extraction in phosphorene-based materials,[3] this is the first report on PNR-mediated hole extraction in any optoelectronic application using discrete nanoribbons. Future theoretical and experimental studies will help further develop the mechanisms put forward in this work and assist in expanding prospective electronic applications incorporating PNRs.

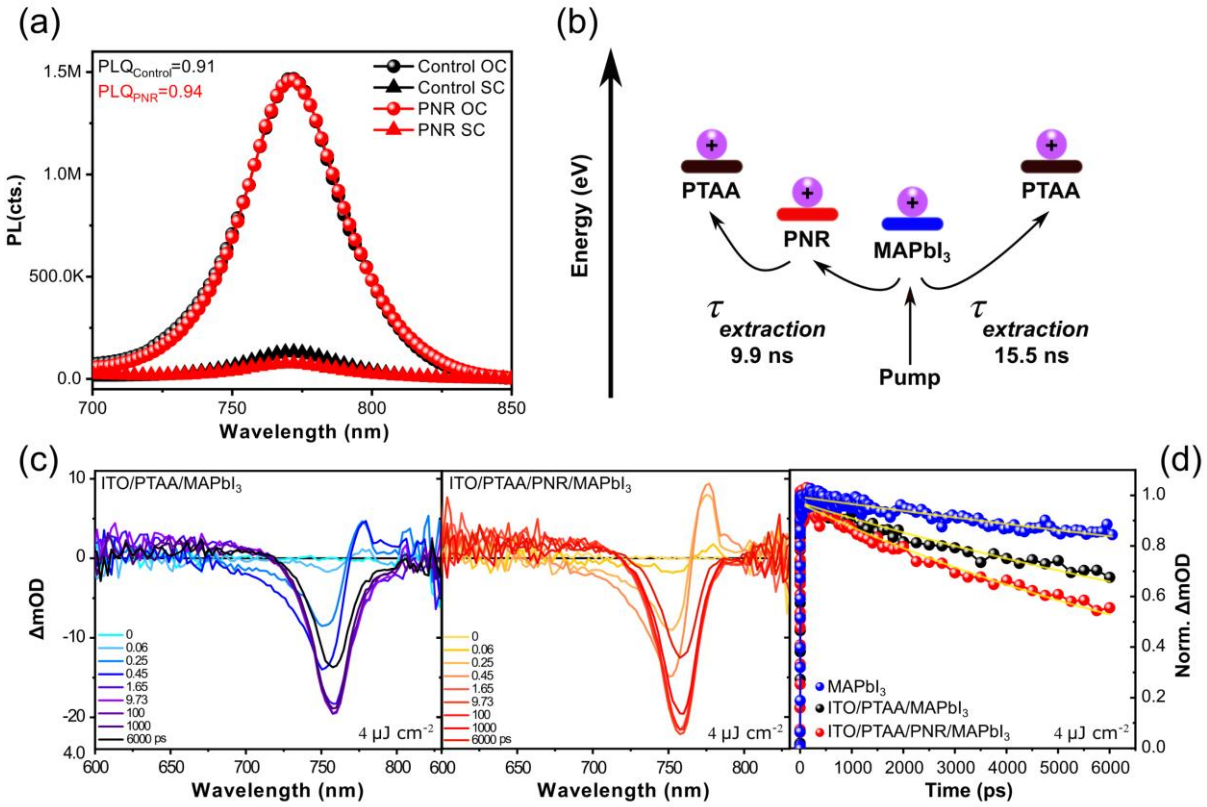

Figure 4. (a) Device PL of control and PNR PSCs at open circuit and short circuit conditions under 1-Sun equivalent laser illumination , (b) proposed schematic of enhanced hole extraction with PNRs, (c) transient absorption spectra evolution within 6 ns of control and PNR films at a pump fluence of 4 μJ cm^{-2}, (d) normalized transient absorption spectra of the band-edge transition in $MAPbI_3$ recorded at the maximum PB bleach signal after two pump excitation of 4 μJ cm^{-2}.

Conclusion

In conclusion, we have demonstrated that PNRs can provide enhanced hole extraction in inverted PSCs by inserting an ultrathin layer between PTAA and the perovskite, resulting in reduced recombination losses, which led to PSCs with FFs exceeding 0.83 and PCEs above 21%. We also demonstrate that our approach can be applied to MA-free PSCs, where PNRs routinely improved PV performance of the inverted PSCs above 20%. In both cases, the efficiency enhancement was mostly ascribable to a significantly improved J_{SC} and FF. SCLC

hole-only device analysis also revealed that the incorporation of PNRs improved both the conductivity and mobility of the PTAA, further demonstrating the potential for PNRs improving hole extraction in universal optoelectronic applications. By virtue of device PL, we show that devices with PNRs show more effective carrier extraction and lower defect densities contributing to higher average efficiencies compared to control cells. Probing the charge transfer dynamics using fs-TAS revealed that films with PNRs show faster decay kinetics with a lifetime of 9.9 ns, compared to control films with lifetimes of 15.5 ns. Faster decay kinetics measured from fs-TAS, aligned well with both the steady-state and time-resolved PL measurements, revealing faster hole extraction from the perovskite to the PTAA when PNRs were employed. As the first example of PNRs in optoelectronic devices, this work opens up new opportunities for future theoretical and alternative experimental applications employing this novel nanomaterial.

Experimental Section

Characterization

Cyclic voltammetry: Tetraethylammonium hexafluorophosphate was used as the salt with PNRs (3 mg/ml) in DMF. A glassy carbon electrode was used as the working electrode, a Pt wire as counter and Ag/AgNO3 reference electrode was also used. Ar gas was blown over the solution whilst CVs were performed. The scan rate was set at 1 mV/s, with 10 scans averaged to obtain the observed trace.

Spectroscopy: Raman spectroscopy was performed on a Renishaw InVia spectrometer fitted with a 785 nm laser. LiP_8 crystals were wax-sealed in a quartz capillary. PTAA was spin coated onto plasma-cleaned glass cover slips using the above procedure below, and PNRs were spin coated 4 times (as for the ‘PNR-4’ devices) onto the PTAA film. PNR films were

removed from the glovebox and measured in air immediately. Photoluminescence and absorption spectra were obtained using a Horiba FL 1039 and Shimadazu UV-2600, respectively. A 635 nm continuous-wave laser purchased from THORLABS adjusted to different light intensities was used for excitation. Specifically, the 1 sun equivalent intensity was calibrated by matching the current under laser illumination with the AM1.5 illumination from solar simulator. A mask was used during the measurement. The TCSPC measurements were conducted by a Delta Flex system (detector: PPD-900, Horiba scientific). A 635 nm laser diode with < 200 ps pulse duration (NanoLED N-02B, Horiba scientific) was used to achieve the excitation with repetition rate of 1 MHz and fluence of 0.64 nJ cm^{-2} $pulse^{-1}$. Ultrafast transient absorption spectra and kinetics were recorded using a HELIOS transient absorption spectrometer with a 630 nm excitation source generated by an optical parametric amplifier (TOPAS Prime from Spectra-Physics) and a frequency mixer (NirUVis from Light Conversion). The white light probe pulse was generated through a sapphire crystal. Both pump and probe light were seeded by a Solstice Ti:Sapphire regenerative amplifier (Newport, Spectra-Physics), with a resulting system instrument response time of 200 fs. The excitation density of the pump beam was monitored by VEGA energy meter (OPHIR Photonics) at a repetition rate of 500 Hz.

Electron Microscopy: TEM micrographs were taken on a JOEL JEM 2100 with an LaB_6 source operated at 200 kV. Samples were prepared by drop casting neat PNR solution onto QUANTIFOIL® holey/continuous carbon 200- or 300-mesh copper or gold TEM grids (EM Resolutions). During transfer to the TEM chamber, the grids were exposed to air for ~ 2 min (for mounting in the holder) and ~ 5 min (for evacuating the holder) before insertion in the microscope. Scanning electron microscopy (SEM) was used to study the cross-sectional morphology of the devices. To reduce charging effects and improve image quality, cross-

sections were sputtered with 10 nm of chromium. SEM images were acquired via an in-lens electron detector using a LEO Gemini 1525 field emission SEM operated at 3 kV.

Solar Cell Characterization: J–V measurements were carried out between one sun (AM 1.5G) and 0.1 suns illumination using a calibrated solar simulator with a Xenon lamp (LOT) and neutral density filters. Device performance was measured with a Keithley 2400 source meter by scanning at 50 mV s^{-1}. Each device contained four pixels which were measured using masks of 0.045 and 0.09 cm^2. EQE measurements were carried out with a halogen lamp chopped to a frequency of 188 Hz through a Newport monochromator and a 4-point probe in connection with a lock-in amplifier was used to collect data. The monochromatic beam was calibrated using a silicon photodiode and the data was analyzed with Tracer 3.2 software (LOT) to produce the EQE spectra.

Material Preparation

PNR solutions: Procedure adapted from Watts *et al*.[14] Back phosphorus crystals (Smart Elements) were outgassed (~10^{-7} mbar), transferred to an argon-filled glovebox and ground with pestle and mortar to ~1-5 mm crystals. The phosphorus (250 mg) and freshly cut lithium (7.5 mg, Sigma Aldrich, 99.9%) were placed in a glass tube fitted with a Swagelok valve, cooled to -50 °C, and placed under vacuum (~10^{-6} mbar). Ammonia gas (Sigma Aldrich 99.99%, cleaned by previous condensation over lithium metal) was condensed to cover the phosphorus and left for 12 h. The ammonia was removed and the LiP_8 crystals were dried under vacuum (10^{-6} mbar) for 1 h, before transferring to the glovebox. In a tight-sealing vial, LiP_8 (7 mg) was added to NMP (7 mL, Sigma Aldrich, 99% anhydrous, dried further with 3 Å molecular sieves), and sonicated for 30 min before centrifuging (~100*g*, 30 min) and decanting to give the PNR solution.

Perovskite solutions: 1.5 M $MAPbI_3$ was prepared by dissolving PbI_2 (TCI, 99.99%) and CH_3NH_3I (Dyesol, 99.99%) at a molar ratio of 1:1 in anhydrous N,N-dimethylformamide (DMF)/ dimethylsulfoxide (DMSO) (9:1.1 volume ratio). 1.25 M $FA_{0.95}Cs_{0.05}PbI_3$ was prepared by dissolving PbI_2 (TCI, 99.99%), CH_5IN_2 (Dyesol, 99.99%), CsI (Alfa Aesar, 99.9%) at a molar ratio of 1:0.95:0.05 in anhydrous DMF/NMP (4:1 volume ratio). We would like to highlight that both perovskite solutions were prepared *via* the Lewis-base adduct of lead(II) iodide for both $MAPbI_3$[72] and $FA_{0.95}Cs_{0.05}PbI_3$,[73] which we find to be highly reproducible.

Device Fabrication

Solar Cell fabrication: ITO was sequentially ultrasonically cleaned in acetone, Milli-Q water, acetone, and iso-propanol for 10 min in each solvent. The ITO was then dried with nitrogen and treated by oxygen plasma for 7 minutes. PTAA (Ossila 14,000 mW, 2.5 mg mL^{-1} in toluene) was then spin-coated on the ITO at 5000 rpm (acceleration of 5000 rpm) for 20s. An ultrathin layer of PFN-Br (1-Material, 0.01 wt% in methanol) was then spin-coated on top of the PTAA at 5000 rpm (acceleration of 5000 rpm) for 20s. PNRs in DMF were spin-coated on top of the HTL at 4000 rpm (acceleration of 5000 rpm) for 30 s and immediately annealed at 100 °C for 30 min to remove DMF. If NMP was employed as the PNR solvent, gentle vacuum was required (in addition to heating) to remove excess solvent. $MAPbI_3$ was spin-coated on the HTL at 4000 rpm (acceleration of 4000 rpm) for 20 s and after 7 s, 0.4 mL of diethyl ether was rapidly dropped on top of the spinning substrate. The substrate was then immediately annealed at 65 °C for 2 min before further annealing at 100 °C for 60 min. When $FA_{0.95}Cs_{0.05}PbI_3$ was used as an absorber layer, it was spin-coated on the HTL at 4000 rpm (acceleration of 4000 rpm) for 20 s and after 10 s, 0.4 mL of diethyl ether was rapidly dropped on top of the spinning substrate. The substrate was then immediately annealed at 65 °C for 2 min before further annealing 150 °C for 15 min. After annealing, all films were

glassy black and allowed to cool for 10 min before deposition of the ETL. PCBM (Solenne 99.5% purity, 30 mg mL^{-1} in chlorobenzene) was then spin-coated on top of the perovskite layer at 2000 rpm (acceleration of 4000 rpm) for 20 s. BCP (Lumtec 99.5% purity, 0.5 mg mL^{-1} in methanol) was then spin-coated on top of the PCBM layer at 5000 rpm (acceleration of 4000 rpm) for 20 s. Immediately after BCP was deposited, the substrates were transferred (under nitrogen) to another glovebox and subject to thermal evaporation. Finally, 100 nm of Cu was thermally evaporated as a top contact at a base pressure of 5×10^{-6} mbar. For open-circuit stability measurements, 100 nm Au was thermally evaporated instead of Cu at the same base pressure.

SCLC hole-only device fabrication: ITO was cleaned as per the description above. PEDOT:PSS (Hercules) was filtered and spin-coated onto ITO at 5000 rpm (acceleration of 4000 rpm) for 45 s and annealed for 30 min at 150 °C. A 600 nm thick layer of PTAA (Ossila 14,000 mW, 100 mg mL^{-1} in toluene) was then spin-coated on top of the PEDOT:PSS at 2000 rpm (acceleration of 1000 rpm). For samples with PNRs, the PNRs were spin-coated on top of the PTAA as per the methods described above. Finally, 100 nm of Au was thermally evaporated as a top contact at a base pressure of 5×10^{-6} mbar.

Acknowledgements

T.J.M would like to thank both the Ramsay Memorial Trust and Royal Commission for the Exhibition of 1851 for their financial support through a Research Fellowship. A.J.C would like to thank the Ramsay Memorial Trust for funding. W.X would like to thank the financial support from China Scholarship Council-Imperial scholarship. L.M acknowledges EPSRC Centre for Doctoral Training in Plastic Electronic Materials EP/L016702/1 for their support. A.A thanks the Winton Program for the Physics of Sustainability and the Gates Scholarship Foundation for financial support. R.P thanks Clare College, University of Cambridge for

financial support. A.A and R.P thank Victor Gray for assistance with CV measurements and advice. J.R.D would like to acknowledge support from UKRI GCRF project SUNRISE (EP/P032591/1) and EPSRC project ATIP (EP/TO28513/1). S.A.H acknowledges support from EPSRC (grant numbers EP/R020574/1 and EP/R023581/1). C.A.H thanks the UK, Engineering and Physical Sciences Research Council for funding.

References

(1) Li, L.; Yu, Y.; Ye, G. J.; Ge, Q.; Ou, X.; Wu, H.; Feng, D.; Chen, X. H.; Zhang, Y. Black Phosphorus Field-Effect Transistors. *Nat. Nanotechnol.* **2014**, *9* (5), 372–377. https://doi.org/10.1038/nnano.2014.35.

(2) Qiao, J.; Kong, X.; Hu, Z.-X.; Yang, F.; Ji, W. High-Mobility Transport Anisotropy and Linear Dichroism in Few-Layer Black Phosphorus. *Nat. Commun.* **2014**, *5* (1), 4475. https://doi.org/10.1038/ncomms5475.

(3) Liu, H.; Neal, A. T.; Zhu, Z.; Luo, Z.; Xu, X.; Tománek, D.; Ye, P. D. Phosphorene: An Unexplored 2D Semiconductor with a High Hole Mobility. *ACS Nano* **2014**, *8* (4), 4033–4041. https://doi.org/10.1021/nn501226z.

(4) Xia, F.; Wang, H.; Jia, Y. Rediscovering Black Phosphorus as an Anisotropic Layered Material for Optoelectronics and Electronics. *Nat. Commun.* **2014**, *5* (1), 4458. https://doi.org/10.1038/ncomms5458.

(5) Li, W.; Yang, Y.; Zhang, G.; Zhang, Y.-W. Ultrafast and Directional Diffusion of Lithium in Phosphorene for High-Performance Lithium-Ion Battery. *Nano Lett.* **2015**, *15* (3), 1691–1697. https://doi.org/10.1021/nl504336h.

(6) Xu, R.; Zhang, S.; Wang, F.; Yang, J.; Wang, Z.; Pei, J.; Myint, Y. W.; Xing, B.; Yu, Z.; Fu, L.; Qin, Q.; Lu, Y. Extraordinarily Bound Quasi-One-Dimensional Trions in Two-Dimensional Phosphorene Atomic Semiconductors. *ACS Nano* **2016**, *10* (2), 2046–2053. https://doi.org/10.1021/acsnano.5b06193.

(7) Zhao, S.; Kang, W.; Xue, J. The Potential Application of Phosphorene as an Anode Material in Li-Ion Batteries. *J. Mater. Chem. A* **2014**, *2* (44), 19046–19052. https://doi.org/10.1039/C4TA04368E.

(8) Liu, Z.; Sun, Y.; Cao, H.; Xie, D.; Li, W.; Wang, J.; Cheetham, A. K. Unzipping of Black Phosphorus to Form Zigzag-Phosphorene Nanobelts. *Nat. Commun.* **2020**, *11* (1), 3917. https://doi.org/10.1038/s41467-020-17622-6.

(9) Carvalho, A.; Wang, M.; Zhu, X.; Rodin, A. S.; Su, H.; Castro Neto, A. H. Phosphorene: From Theory to Applications. *Nat. Rev. Mater.* **2016**, *1* (11), 1–16. https://doi.org/10.1038/natrevmats.2016.61.

(10) Batmunkh, M.; Bat-Erdene, M.; Shapter, J. G. Phosphorene and Phosphorene-Based Materials – Prospects for Future Applications. *Adv. Mater.* **2016**, *28* (39), 8586–8617. https://doi.org/10.1002/adma.201602254.

(11) Taghizadeh Sisakht, E.; Zare, M. H.; Fazileh, F. Scaling Laws of Band Gaps of Phosphorene Nanoribbons: A Tight-Binding Calculation. *Phys. Rev. B* **2015**, *91* (8), 085409. https://doi.org/10.1103/PhysRevB.91.085409.

(12) Zhang, J.; Liu, H. J.; Cheng, L.; Wei, J.; Liang, J. H.; Fan, D. D.; Shi, J.; Tang, X. F.; Zhang, Q. J. Phosphorene Nanoribbon as a Promising Candidate for Thermoelectric Applications. *Sci. Rep.* **2014**, *4* (1), 1–8. https://doi.org/10.1038/srep06452.
(13) Soleimanikahnoj, S.; Knezevic, I. Pseudospin Electronics in Phosphorene Nanoribbons. *Phys. Rev. Appl.* **2017**, *8* (6), 064021. https://doi.org/10.1103/PhysRevApplied.8.064021.
(14) Watts, M. C.; Picco, L.; Russell-Pavier, F. S.; Cullen, P. L.; Miller, T. S.; Bartuś, S. P.; Payton, O. D.; Skipper, N. T.; Tileli, V.; Howard, C. A. Production of Phosphorene Nanoribbons. *Nature* **2019**, *568* (7751), 216–220. https://doi.org/10.1038/s41586-019-1074-x.
(15) Lee, S.; Yang, F.; Suh, J.; Yang, S.; Lee, Y.; Li, G.; Sung Choe, H.; Suslu, A.; Chen, Y.; Ko, C.; Park, J.; Liu, K.; Li, J.; Hippalgaonkar, K.; Urban, J. J.; Tongay, S.; Wu, J. Anisotropic In-Plane Thermal Conductivity of Black Phosphorus Nanoribbons at Temperatures Higher than 100 K. *Nat. Commun.* **2015**, *6* (1), 8573. https://doi.org/10.1038/ncomms9573.
(16) Masih Das, P.; Danda, G.; Cupo, A.; Parkin, W. M.; Liang, L.; Kharche, N.; Ling, X.; Huang, S.; Dresselhaus, M. S.; Meunier, V.; Drndić, M. Controlled Sculpture of Black Phosphorus Nanoribbons. *ACS Nano* **2016**, *10* (6), 5687–5695. https://doi.org/10.1021/acsnano.6b02435.
(17) Feng, X.; Huang, X.; Chen, L.; Tan, W. C.; Wang, L.; Ang, K.-W. High Mobility Anisotropic Black Phosphorus Nanoribbon Field-Effect Transistor. *Adv. Funct. Mater.* **2018**, *28* (28), 1801524. https://doi.org/10.1002/adfm.201801524.
(18) Yu, W.; Yang, J.; Li, J.; Zhang, K.; Xu, H.; Zhou, X.; Chen, W.; Loh, K. P. Facile Production of Phosphorene Nanoribbons towards Application in Lithium Metal Battery. *Adv. Mater.* **2021**, *n/a* (n/a), 2102083. https://doi.org/10.1002/adma.202102083.
(19) Lee, M. M.; Teuscher, J.; Miyasaka, T.; Murakami, T. N.; Snaith, H. J. Efficient Hybrid Solar Cells Based on Meso-Superstructured Organometal Halide Perovskites. *Science* **2012**, *338* (6107), 643–647. https://doi.org/10.1126/science.1228604.
(20) Etgar, L.; Gao, P.; Xue, Z.; Peng, Q.; Chandiran, A. K.; Liu, B.; Nazeeruddin, Md. K.; Grätzel, M. Mesoscopic CH3NH3PbI3/TiO2 Heterojunction Solar Cells. *J. Am. Chem. Soc.* **2012**, *134* (42), 17396–17399. https://doi.org/10.1021/ja307789s.
(21) Stranks, S. D.; Eperon, G. E.; Grancini, G.; Menelaou, C.; Alcocer, M. J. P.; Leijtens, T.; Herz, L. M.; Petrozza, A.; Snaith, H. J. Electron-Hole Diffusion Lengths Exceeding 1 Micrometer in an Organometal Trihalide Perovskite Absorber. *Science* **2013**, *342* (6156), 341–344. https://doi.org/10.1126/science.1243982.
(22) Xing, G.; Mathews, N.; Sun, S.; Lim, S. S.; Lam, Y. M.; Grätzel, M.; Mhaisalkar, S.; Sum, T. C. Long-Range Balanced Electron- and Hole-Transport Lengths in Organic-Inorganic CH3NH3PbI3. *Science* **2013**, *342* (6156), 344–347. https://doi.org/10.1126/science.1243167.
(23) Eperon, G. E.; Stranks, S. D.; Menelaou, C.; Johnston, M. B.; Herz, L. M.; Snaith, H. J. Formamidinium Lead Trihalide: A Broadly Tunable Perovskite for Efficient Planar Heterojunction Solar Cells. *Energy Environ. Sci.* **2014**, *7* (3), 982–988. https://doi.org/10.1039/C3EE43822H.
(24) Li, Y.; Meng, L.; Yang, Y. (Michael); Xu, G.; Hong, Z.; Chen, Q.; You, J.; Li, G.; Yang, Y.; Li, Y. High-Efficiency Robust Perovskite Solar Cells on Ultrathin Flexible Substrates. *Nat. Commun.* **2016**, *7* (1), 1–10. https://doi.org/10.1038/ncomms10214.
(25) Saliba, M.; Matsui, T.; Seo, J.-Y.; Domanski, K.; Correa-Baena, J.-P.; Nazeeruddin, M. K.; Zakeeruddin, S. M.; Tress, W.; Abate, A.; Hagfeldt, A.; Grätzel, M. Cesium-Containing

Triple Cation Perovskite Solar Cells: Improved Stability, Reproducibility and High Efficiency. *Energy Environ. Sci.* **2016**, *9* (6), 1989–1997. https://doi.org/10.1039/C5EE03874J.

(26) Wang, P.; Li, R.; Chen, B.; Hou, F.; Zhang, J.; Zhao, Y.; Zhang, X. Gradient Energy Alignment Engineering for Planar Perovskite Solar Cells with Efficiency Over 23%. *Adv. Mater.* **2020**, *32* (6), 1905766. https://doi.org/10.1002/adma.201905766.

(27) Cai, M.; Wu, Y.; Chen, H.; Yang, X.; Qiang, Y.; Han, L. Cost-Performance Analysis of Perovskite Solar Modules. *Adv. Sci.* **2017**, *4* (1), 1600269. https://doi.org/10.1002/advs.201600269.

(28) Vaitukaityte, D.; Wang, Z.; Malinauskas, T.; Magomedov, A.; Bubniene, G.; Jankauskas, V.; Getautis, V.; Snaith, H. J. Efficient and Stable Perovskite Solar Cells Using Low-Cost Aniline-Based Enamine Hole-Transporting Materials. *Adv. Mater.* **2018**, *30* (45), 1803735. https://doi.org/10.1002/adma.201803735.

(29) Batmunkh, M.; Macdonald, T. J.; Peveler, W. J.; Bati, A. S. R.; Carmalt, C. J.; Parkin, I. P.; Shapter, J. G. Plasmonic Gold Nanostars Incorporated into High-Efficiency Perovskite Solar Cells. *ChemSusChem* **2017**, *10* (19), 3750–3753. https://doi.org/10.1002/cssc.201701056.

(30) Macdonald, T. J.; Batmunkh, M.; Lin, C.-T.; Kim, J.; Tune, D. D.; Ambroz, F.; Li, X.; Xu, S.; Sol, C.; Papakonstantinou, I.; McLachlan, M. A.; Parkin, I. P.; Shapter, J. G.; Durrant, J. R. Origin of Performance Enhancement in TiO2-Carbon Nanotube Composite Perovskite Solar Cells. *Small Methods* **2019**, *3* (10), 1900164. https://doi.org/10.1002/smtd.201900164.

(31) Bati, A. S. R.; Hao, M.; Macdonald, T. J.; Batmunkh, M.; Yamauchi, Y.; Wang, L.; Shapter, J. G. 1D-2D Synergistic MXene-Nanotubes Hybrids for Efficient Perovskite Solar Cells. *Small* **2021**, *n/a* (n/a), 2101925. https://doi.org/10.1002/smll.202101925.

(32) Cai, Y.; Zhang, G.; Zhang, Y.-W. Layer-Dependent Band Alignment and Work Function of Few-Layer Phosphorene. *Sci. Rep.* **2014**, *4* (1), 6677. https://doi.org/10.1038/srep06677.

(33) Chen, W.; Li, K.; Wang, Y.; Feng, X.; Liao, Z.; Su, Q.; Lin, X.; He, Z. Black Phosphorus Quantum Dots for Hole Extraction of Typical Planar Hybrid Perovskite Solar Cells. *J. Phys. Chem. Lett.* **2017**, *8* (3), 591–598. https://doi.org/10.1021/acs.jpclett.6b02843.

(34) Muduli, S. K.; Varrla, E.; Kulkarni, S. A.; Han, G.; Thirumal, K.; Lev, O.; Mhaisalkar, S.; Mathews, N. 2D Black Phosphorous Nanosheets as a Hole Transporting Material in Perovskite Solar Cells. *J. Power Sources* **2017**, *371*, 156–161. https://doi.org/10.1016/j.jpowsour.2017.10.018.

(35) Fu, N.; Huang, C.; Lin, P.; Zhu, M.; Li, T.; Ye, M.; Lin, S.; Zhang, G.; Du, J.; Liu, C.; Xu, B.; Wang, D.; Ke, S. Black Phosphorus Quantum Dots as Dual-Functional Electron-Selective Materials for Efficient Plastic Perovskite Solar Cells. *J. Mater. Chem. A* **2018**, *6* (19), 8886–8894. https://doi.org/10.1039/C8TA01408F.

(36) Batmunkh, M.; Vimalanathan, K.; Wu, C.; Bati, A. S. R.; Yu, L.; Tawfik, S. A.; Ford, M. J.; Macdonald, T. J.; Raston, C. L.; Priya, S.; Gibson, C. T.; Shapter, J. G. Efficient Production of Phosphorene Nanosheets via Shear Stress Mediated Exfoliation for Low-Temperature Perovskite Solar Cells. *Small Methods* **2019**, *3* (5), 1800521. https://doi.org/10.1002/smtd.201800521.

(37) Zhang, M.; Ye, M.; Wang, W.; Ma, C.; Wang, S.; Liu, Q.; Lian, T.; Huang, J.; Lin, Z. Synergistic Cascade Carrier Extraction via Dual Interfacial Positioning of Ambipolar Black Phosphorene for High-Efficiency Perovskite Solar Cells. *Adv. Mater.* **2020**, *32* (28), 2000999. https://doi.org/10.1002/adma.202000999.

(38) Tran, V.; Soklaski, R.; Liang, Y.; Yang, L. Layer-Controlled Band Gap and Anisotropic Excitons in Few-Layer Black Phosphorus. *Phys. Rev. B* **2014**, *89* (23), 235319. https://doi.org/10.1103/PhysRevB.89.235319.

(39) Lin, C.-T.; Lee, J.; Kim, J.; Macdonald, T. J.; Ngiam, J.; Xu, B.; Daboczi, M.; Xu, W.; Pont, S.; Park, B.; Kang, H.; Kim, J.-S.; Payne, D. J.; Lee, K.; Durrant, J. R.; McLachlan, M. A. Origin of Open-Circuit Voltage Enhancements in Planar Perovskite Solar Cells Induced by Addition of Bulky Organic Cations. *Adv. Funct. Mater.* **2020**, *30* (7), 1906763. https://doi.org/10.1002/adfm.201906763.

(40) Lee, J.; Kang, H.; Kim, G.; Back, H.; Kim, J.; Hong, S.; Park, B.; Lee, E.; Lee, K. Achieving Large-Area Planar Perovskite Solar Cells by Introducing an Interfacial Compatibilizer. *Adv. Mater.* **2017**, *29* (22), 1606363. https://doi.org/10.1002/adma.201606363.

(41) Vogel, M.; Doka, S.; Breyer, Ch.; Lux-Steiner, M. Ch.; Fostiropoulos, K. On the Function of a Bathocuproine Buffer Layer in Organic Photovoltaic Cells. *Appl. Phys. Lett.* **2006**, *89* (16), 163501. https://doi.org/10.1063/1.2362624.

(42) Lin, C.-T.; Ngiam, J.; Xu, B.; Chang, Y.-H.; Du, T.; Macdonald, T. J.; Durrant, J. R.; McLachlan, M. A. Enhancing the Operational Stability of Unencapsulated Perovskite Solar Cells through Cu–Ag Bilayer Electrode Incorporation. *J. Mater. Chem. A* **2020**, *8* (17), 8684–8691. https://doi.org/10.1039/D0TA01606C.

(43) Alsalloum, A. Y.; Turedi, B.; Zheng, X.; Mitra, S.; Zhumekenov, A. A.; Lee, K. J.; Maity, P.; Gereige, I.; AlSaggaf, A.; Roqan, I. S.; Mohammed, O. F.; Bakr, O. M. Low-Temperature Crystallization Enables 21.9% Efficient Single-Crystal MAPbI3 Inverted Perovskite Solar Cells. *ACS Energy Lett.* **2020**, *5* (2), 657–662. https://doi.org/10.1021/acsenergylett.9b02787.

(44) Habisreutinger, S. N.; Noel, N. K.; Snaith, H. J. Hysteresis Index: A Figure without Merit for Quantifying Hysteresis in Perovskite Solar Cells. *ACS Energy Lett.* **2018**, *3* (10), 2472–2476. https://doi.org/10.1021/acsenergylett.8b01627.

(45) Wu, C.-G.; Chiang, C.-H.; Tseng, Z.-L.; Nazeeruddin, M. K.; Hagfeldt, A.; Grätzel, M. High Efficiency Stable Inverted Perovskite Solar Cells without Current Hysteresis. *Energy Environ. Sci.* **2015**, *8* (9), 2725–2733. https://doi.org/10.1039/C5EE00645G.

(46) Liu, X.; Cheng, Y.; Liu, C.; Zhang, T.; Zhang, N.; Zhang, S.; Chen, J.; Xu, Q.; Ouyang, J.; Gong, H. 20.7% Highly Reproducible Inverted Planar Perovskite Solar Cells with Enhanced Fill Factor and Eliminated Hysteresis. *Energy Environ. Sci.* **2019**, *12* (5), 1622–1633. https://doi.org/10.1039/C9EE00872A.

(47) Saliba, M.; Etgar, L. Current Density Mismatch in Perovskite Solar Cells. *ACS Energy Lett.* **2020**, *5* (9), 2886–2888. https://doi.org/10.1021/acsenergylett.0c01642.

(48) Mihailetchi, V. D.; Wildeman, J.; Blom, P. W. M. Space-Charge Limited Photocurrent. *Phys. Rev. Lett.* **2005**, *94* (12), 126602. https://doi.org/10.1103/PhysRevLett.94.126602.

(49) Singh, T.; Miyasaka, T. Stabilizing the Efficiency Beyond 20% with a Mixed Cation Perovskite Solar Cell Fabricated in Ambient Air under Controlled Humidity. *Adv. Energy Mater.* **2017**, *8* (3), 1700677. https://doi.org/10.1002/aenm.201700677.

(50) Cowan, S. R.; Roy, A.; Heeger, A. J. Recombination in Polymer-Fullerene Bulk Heterojunction Solar Cells. *Phys. Rev. B* **2010**, *82* (24), 245207. https://doi.org/10.1103/PhysRevB.82.245207.

(51) Wetzelaer, G.-J. A. H.; Scheepers, M.; Sempere, A. M.; Momblona, C.; Ávila, J.; Bolink, H. J. Trap-Assisted Non-Radiative Recombination in Organic–Inorganic Perovskite Solar Cells. *Adv. Mater.* **2015**, *27* (11), 1837–1841. https://doi.org/10.1002/adma.201405372.

(52) Tress, W.; Yavari, M.; Domanski, K.; Yadav, P.; Niesen, B.; Baena, J. P. C.; Hagfeldt, A.; Graetzel, M. Interpretation and Evolution of Open-Circuit Voltage, Recombination, Ideality Factor and Subgap Defect States during Reversible Light-Soaking and Irreversible Degradation of Perovskite Solar Cells. *Energy Environ. Sci.* **2018**, *11* (1), 151–165. https://doi.org/10.1039/C7EE02415K.

(53) Sah, C.; Noyce, R. N.; Shockley, W. Carrier Generation and Recombination in P-N Junctions and P-N Junction Characteristics. *Proc. IRE* **1957**, *45* (9), 1228–1243. https://doi.org/10.1109/JRPROC.1957.278528.

(54) Wetzelaer, G. A. H.; Kuik, M.; Nicolai, H. T.; Blom, P. W. M. Trap-Assisted and Langevin-Type Recombination in Organic Light-Emitting Diodes. *Phys. Rev. B* **2011**, *83* (16), 165204. https://doi.org/10.1103/PhysRevB.83.165204.

(55) Kuik, M.; Koster, L. J. A.; Wetzelaer, G. A. H.; Blom, P. W. M. Trap-Assisted Recombination in Disordered Organic Semiconductors. *Phys. Rev. Lett.* **2011**, *107* (25), 256805. https://doi.org/10.1103/PhysRevLett.107.256805.

(56) Conings, B.; Drijkoningen, J.; Gauquelin, N.; Babayigit, A.; D'Haen, J.; D'Olieslaeger, L.; Ethirajan, A.; Verbeeck, J.; Manca, J.; Mosconi, E.; Angelis, F. D.; Boyen, H.-G. Intrinsic Thermal Instability of Methylammonium Lead Trihalide Perovskite. *Adv. Energy Mater.* **2015**, *5* (15), 1500477. https://doi.org/10.1002/aenm.201500477.

(57) Wang, S.; Jiang, Y.; Juarez-Perez, E. J.; Ono, L. K.; Qi, Y. Accelerated Degradation of Methylammonium Lead Iodide Perovskites Induced by Exposure to Iodine Vapour. *Nat. Energy* **2016**, *2* (1), 1–8. https://doi.org/10.1038/nenergy.2016.195.

(58) Lin, Y.-H.; Sakai, N.; Da, P.; Wu, J.; Sansom, H. C.; Ramadan, A. J.; Mahesh, S.; Liu, J.; Oliver, R. D. J.; Lim, J.; Aspitarte, L.; Sharma, K.; Madhu, P. K.; Morales-Vilches, A. B.; Nayak, P. K.; Bai, S.; Gao, F.; Grovenor, C. R. M.; Johnston, M. B.; Labram, J. G.; Durrant, J. R.; Ball, J. M.; Wenger, B.; Stannowski, B.; Snaith, H. J. A Piperidinium Salt Stabilizes Efficient Metal-Halide Perovskite Solar Cells. *Science* **2020**, *369* (6499), 96–102. https://doi.org/10.1126/science.aba1628.

(59) Li, D.; Huang, Y.; Wang, G.; Lian, Q.; Shi, R.; Zhang, L.; Wang, X.; Gao, F.; Kong, W.; Xu, B.; Cheng, C.; Li, S. Boosting the Performance of MA-Free Inverted Perovskite Solar Cells via Multifunctional Ion Liquid. *J. Mater. Chem. A* **2021**, *9* (21), 12746–12754. https://doi.org/10.1039/D1TA01883C.

(60) Lampert, M. A.; Mark, P. *Current Injection in Solids*; Academic Press: New York; London, 1970.

(61) Murgatroyd, P. N. Theory of Space-Charge-Limited Current Enhanced by Frenkel Effect. *J. Phys. Appl. Phys.* **1970**, *3* (2), 151–156. https://doi.org/10.1088/0022-3727/3/2/308.

(62) Gasparini, N.; Righi, S.; Tinti, F.; Savoini, A.; Cominetti, A.; Po, R.; Camaioni, N. Neat C70-Based Bulk-Heterojunction Polymer Solar Cells with Excellent Acceptor Dispersion. *ACS Appl. Mater. Interfaces* **2014**, *6* (23), 21416–21425. https://doi.org/10.1021/am506394m.

(63) Seo, J.-Y.; Kim, H.-S.; Akin, S.; Stojanovic, M.; Simon, E.; Fleischer, M.; Hagfeldt, A.; Zakeeruddin, S. M.; Grätzel, M. Novel P-Dopant toward Highly Efficient and Stable Perovskite Solar Cells. *Energy Environ. Sci.* **2018**, *11* (10), 2985–2992. https://doi.org/10.1039/C8EE01500G.

(64) Luo, J.; Xia, J.; Yang, H.; Chen, L.; Wan, Z.; Han, F.; Malik, H. A.; Zhu, X.; Jia, C. Toward High-Efficiency, Hysteresis-Less, Stable Perovskite Solar Cells: Unusual Doping of a Hole-Transporting Material Using a Fluorine-Containing Hydrophobic Lewis Acid. *Energy Environ. Sci.* **2018**, *11* (8), 2035–2045. https://doi.org/10.1039/C8EE00036K.

(65) Rombach, F. M.; Haque, S. A.; Macdonald, T. J. Lessons Learned from Spiro-OMeTAD and PTAA in Perovskite Solar Cells. *Energy Environ. Sci.* **2021**. https://doi.org/10.1039/D1EE02095A.
(66) Obrzut, J.; Page, K. A. Electrical Conductivity and Relaxation in Poly(3-Hexylthiophene). *Phys. Rev. B* **2009**, *80* (19), 195211. https://doi.org/10.1103/PhysRevB.80.195211.
(67) Du, T.; Xu, W.; Daboczi, M.; Kim, J.; Xu, S.; Lin, C.-T.; Kang, H.; Lee, K.; J. Heeney, M.; Kim, J.-S.; R. Durrant, J.; A. McLachlan, M. P-Doping of Organic Hole Transport Layers in p–i–n Perovskite Solar Cells: Correlating Open-Circuit Voltage and Photoluminescence Quenching. *J. Mater. Chem. A* **2019**, *7* (32), 18971–18979. https://doi.org/10.1039/C9TA03896E.
(68) Lin, C.-T.; Xu, W.; Macdonald, T. J.; Ngiam, J.; Kim, J.-H.; Du, T.; Xu, S.; Tuladhar, P. S.; Kang, H.; Lee, K.; Durrant, J. R.; McLachlan, M. A. Correlating the Active Layer Structure and Composition with the Device Performance and Lifetime of Amino-Acid-Modified Perovskite Solar Cells. *ACS Appl. Mater. Interfaces* **2021**, *13* (36), 43505–43515. https://doi.org/10.1021/acsami.1c08279.
(69) Caprioglio, P.; Stolterfoht, M.; Wolff, C. M.; Unold, T.; Rech, B.; Albrecht, S.; Neher, D. On the Relation between the Open-Circuit Voltage and Quasi-Fermi Level Splitting in Efficient Perovskite Solar Cells. *Adv. Energy Mater.* **2019**, *9* (33), 1901631. https://doi.org/10.1002/aenm.201901631.
(70) Price, M. B.; Butkus, J.; Jellicoe, T. C.; Sadhanala, A.; Briane, A.; Halpert, J. E.; Broch, K.; Hodgkiss, J. M.; Friend, R. H.; Deschler, F. Hot-Carrier Cooling and Photoinduced Refractive Index Changes in Organic–Inorganic Lead Halide Perovskites. *Nat. Commun.* **2015**, *6* (1), 8420. https://doi.org/10.1038/ncomms9420.
(71) Shi, D.; Adinolfi, V.; Comin, R.; Yuan, M.; Alarousu, E.; Buin, A.; Chen, Y.; Hoogland, S.; Rothenberger, A.; Katsiev, K.; Losovyj, Y.; Zhang, X.; Dowben, P. A.; Mohammed, O. F.; Sargent, E. H.; Bakr, O. M. Low Trap-State Density and Long Carrier Diffusion in Organolead Trihalide Perovskite Single Crystals. *Science* **2015**, *347* (6221), 519–522. https://doi.org/10.1126/science.aaa2725.
(72) Ahn, N.; Son, D.-Y.; Jang, I.-H.; Kang, S. M.; Choi, M.; Park, N.-G. Highly Reproducible Perovskite Solar Cells with Average Efficiency of 18.3% and Best Efficiency of 19.7% Fabricated via Lewis Base Adduct of Lead(II) Iodide. *J. Am. Chem. Soc.* **2015**, *137* (27), 8696–8699. https://doi.org/10.1021/jacs.5b04930.
(73) Lee, J.-W.; Dai, Z.; Lee, C.; Lee, H. M.; Han, T.-H.; De Marco, N.; Lin, O.; Choi, C. S.; Dunn, B.; Koh, J.; Di Carlo, D.; Ko, J. H.; Maynard, H. D.; Yang, Y. Tuning Molecular Interactions for Highly Reproducible and Efficient Formamidinium Perovskite Solar Cells via Adduct Approach. *J. Am. Chem. Soc.* **2018**, *140* (20), 6317–6324. https://doi.org/10.1021/jacs.8b01037.